

Article

Response of Precipitation in Tianshan to Global Climate Change Based on the Berkeley Earth and ERA5 Reanalysis Products

Mengtian Fan ^{1,2} , Jianhua Xu ^{1,2,*} , Dahui Li ³ and Yaning Chen ⁴

- ¹ Key Laboratory of Geographic Information Science (Ministry of Education), School of Geographic Sciences, East China Normal University, Shanghai 200241, China; 52193901013@stu.ecnu.edu.cn
- ² Research Center for East-West Cooperation in China, East China Normal University, Shanghai 200241, China
- ³ School of Geospatial Engineering and Science, Sun Yat-Sen University, Zhuhai 519082, China; lidh59@mail2.sysu.edu.cn
- ⁴ State Key Laboratory of Desert and Oasis Ecology, Xinjiang Institute of Ecology and Geography, Chinese Academy of Sciences, Urumqi 830011, China; chenyn@ms.xjb.ac.cn
- * Correspondence: jhxu@geo.ecnu.edu.cn

Abstract: Global climate change has readjusted a global-scale precipitation distribution in magnitude and timing. In mountainous areas, meteorological stations and observation data are very limited, making it difficult to accurately understand the response of precipitation to global climate change. Based on ECMWF Reanalysis v5 precipitation products, Berkeley Earth global temperature, and typical atmospheric circulation indexes, we integrated a gradient descent-nonlinear regression down-scaling model, cross wavelet transform, and wavelet correlation method to analyze the precipitation response in Tianshan to global climate change. This study provides a high-resolution (90 m × 90 m) precipitation dataset in Tianshan and confirms that global warming, the North Pacific Pattern (NP), the Western Hemisphere Warm Pool (WHWP), and the Atlantic Multidecadal Oscillation (AMO) are related to the humidification of Tianshan over the past 40 years. The precipitation in Tianshan and global temperature have a resonance period of 8–15 months, and the correlation coefficient is above 0.9. In Tianshan, spring precipitation is determined mainly by AMO, North Tropical Atlantic Sea Level Temperature, Pacific Interdecadal Oscillation (PDO), Tropical North Atlantic Index, WHWP, NP, summer by NP, North Atlantic Oscillation, and PDO, autumn by AMO, and winter by Arctic Oscillation. This research can serve the precipitation forecast of Tianshan and help in the understanding of the regional response to global climate change.

Keywords: response; precipitation; global warming; atmospheric circulation; Tianshan



Citation: Fan, M.; Xu, J.; Li, D.; Chen, Y. Response of Precipitation in Tianshan to Global Climate Change Based on the Berkeley Earth and ERA5 Reanalysis Products. *Remote Sens.* **2022**, *14*, 519. <https://doi.org/10.3390/rs14030519>

Academic Editors: Kenji Nakamura, Atsushi Hamada, Mikiko Fujita and Jungho Kim

Received: 21 December 2021

Accepted: 20 January 2022

Published: 21 January 2022

Publisher's Note: MDPI stays neutral with regard to jurisdictional claims in published maps and institutional affiliations.



Copyright: © 2022 by the authors. Licensee MDPI, Basel, Switzerland. This article is an open access article distributed under the terms and conditions of the Creative Commons Attribution (CC BY) license (<https://creativecommons.org/licenses/by/4.0/>).

1. Introduction

Large increases in surface temperature have been detected over the past few decades [1]. With global warming, global average precipitation has shown an increasing trend [2]. Wentz et al. [3] reported that global mean precipitation increased at a rate of approximately 7.4% per 1 °C between 1987 and 2006. In China, the winter precipitation increased at a rate of 9.7% per 1 °C of surface warming [4]. Global warming has exacerbated the uncertainty of regional precipitation changes [5–7]. Over the past three decades, the differences in seasonal precipitation have become more pronounced [8], and the spatial distributions of precipitation have changed [9]. At the same time, the difference between dry and wet regions expanded [10–12], and significant changes in wet-day frequencies and consecutive dry days have been identified [13]. Moreover, climate models [14] and observations [15,16] show an increase in precipitation extremes. Extreme precipitation is predicted to further increase in the future [17,18], and its spatial pattern is heterogeneous, showing opposite trends in different regions [19].

On a regional scale, atmospheric circulation affects regional precipitation change [20]. In different seasons, there are differences in the response of precipitation to circulation changes [21]. In summer, there is a significant positive correlation between Arctic Oscillation and precipitation, and in winter, there is a significant positive correlation between North Atlantic Oscillation and precipitation in Tianshan [5]. In addition, changes in regional precipitation are not synchronized with that in circulation. Song et al. [22] found that winter North Atlantic Oscillation affects the precipitation in the second summer in South Korea and eastern China. In the Hetao region of northwest China, strong North Atlantic Oscillation in winter may lead to an increase in precipitation of the next summer [23].

In the context of global warming, the water resources system in arid mountainous areas, which are mainly recharged by rainfall, will undergo major changes in temporal and spatial distribution of water resources [24–26]. The precipitation changes in arid mountainous areas are responsible for extreme weather events and lead to potentially disastrous impacts on society, the environment, and ecology [27–29]. Known as the “Central Asian Water Tower”, the Tianshan Mountains are an important water source in the middle section of the Silk Road Economic Belt [27], where precipitation changes affect the stability of the water system and sustainable development in the arid regions of Central Asia [30–32]. In mountainous areas, due to the high altitude and complex terrain, the observed precipitation data are scarce. Reanalysis products, such as Modern-Era Retrospective Analysis for Research and Applications [33], ERA-Interim [34], ECMWF Reanalysis v5 (ERA5) [35], the tropical rainfall measurement mission [36], and the global precipitation climatology project [37,38], provide precipitation datasets continuous in both space and time. Studies have shown that ERA5 precipitation is close to the observations [39–42]. However, owing to the coarse spatial scale ($0.25^\circ \times 0.25^\circ$), reanalysis products are unable to accurately resolve the precipitation changes on a regional scale [43,44].

In order to bridge the scale gap between the coarse scale reanalysis outputs and regional scale precipitation changes, statistical and dynamic downscaling approaches have been developed [5,45]. Compared to dynamic downscaling, statistical downscaling has gained wide popularity due to its low computational cost and simplicity [46]. The techniques widely used in statistical downscaling include Multi Linear Regression [47], Nonlinear Regression [5], Generalized Linear Models [48], Artificial Neural Networks [49], Support Vector Machine [50], and Relevance Vector Machine [51], etc. Sachindra et al. [46] found that irrespective of the climate regime, the SVM and RVM-based precipitation downscaling models showed the best performance with the Polynomial kernel. Vandal et al. [52] suggested that the direct application of state-of-the-art machine learning methods to statistical downscaling does not provide direct improvements over simpler, longstanding approaches. Compared with machine learning such as artificial neural network and support vector regression, traditional regressions require less computation and can display regression coefficients, which could assess the dependence of dependent variables on different factors. In traditional regressions, the least squares method is widely used to calculate regression coefficients, but it is sensitive to noise and suitable for relatively small samples [53,54]. Gradient descent (GD) is often used as the core training algorithm, and it searches for the most significant decline of the cost function in each iteration until the cost function is minimized and stabilized [55,56]. Studies have shown a nonlinear relationship of the precipitation with latitude, longitude and terrain factors in Northwest China [57,58]. Therefore, this study established a nonlinear model for downscaling precipitation, and the GD algorithm was used to train the model.

Selecting the Tianshan Mountains as a target, this study proposed a gradient descent-nonlinear regression (GD-NLR) downscaling model to simulate high-resolution precipitation. Then, based on downscaled data, the Berkeley Earth global temperature and the typical atmospheric circulation index, we analyzed the response of precipitation in the Tianshan Mountains to global climate change. Although many machine learning models have been developed for precipitation downscaling, the accuracy of different models varies greatly, and their applicability in alpine mountains needs further verification. The GD-NLR

model developed in this study can accurately simulate the precipitation changes in the Tianshan Mountains, which provides a new idea for simulating high-resolution precipitation in alpine mountains. In addition, the current literature does not study in detail the response of arid mountainous regions to global climate change. This study reveals the multi-scale response of mountainous precipitation to global warming and circulation changes and identifies the circulations affecting precipitation changes in different seasons. Moreover, predicting future precipitation changes can serve regional water resource management. Based on forecast results, measures could be formulated to deal with possible floods and droughts. This study calculates the lag time of the precipitation change in the Tianshan Mountains relative to typical circulation changes. According to current circulation changes, the future precipitation change in the Tianshan Mountains can be roughly predicted.

2. Materials and Methods

2.1. Study Area

Tianshan is located in the hinterland of Eurasia, stretching across China, Kazakhstan, Kyrgyzstan, and Uzbekistan [59,60]. In this study, we investigated the region between $39^{\circ}18'N$ – $45^{\circ}24'N$ and $73^{\circ}54'E$ – $95^{\circ}18'E$ (Figure 1) [61]. The region stretches for 1700 km, with an average width of 250–350 km and an area of $528,670\text{ km}^2$. It divides Xinjiang, China, into two parts, and the natural geographic landscapes of the north and south are completely different [62]. The terrain in Tianshan is complex, including mountains, valleys and basins, with an average elevation of 4000 m [63]. Due to the high altitude, the construction of meteorological stations is difficult, with less than one station per $10,000\text{ km}^2$ [64]. Tianshan is far from the ocean and is dominated by a typical continental arid and semi-arid climate, with water vapor mainly coming from the Atlantic Ocean [36]. In order to understand the response of precipitation to global climate change in different regions, this study divided the study area into West Tianshan (WTS) ($73^{\circ}54'E$ – $81^{\circ}18'E$), Central Tianshan (CTS) ($81^{\circ}18'E$ – $87^{\circ}30'E$), and Eastern Tianshan (ETS) ($87^{\circ}30'E$ – $95^{\circ}18'E$) (Figure 1) [65].

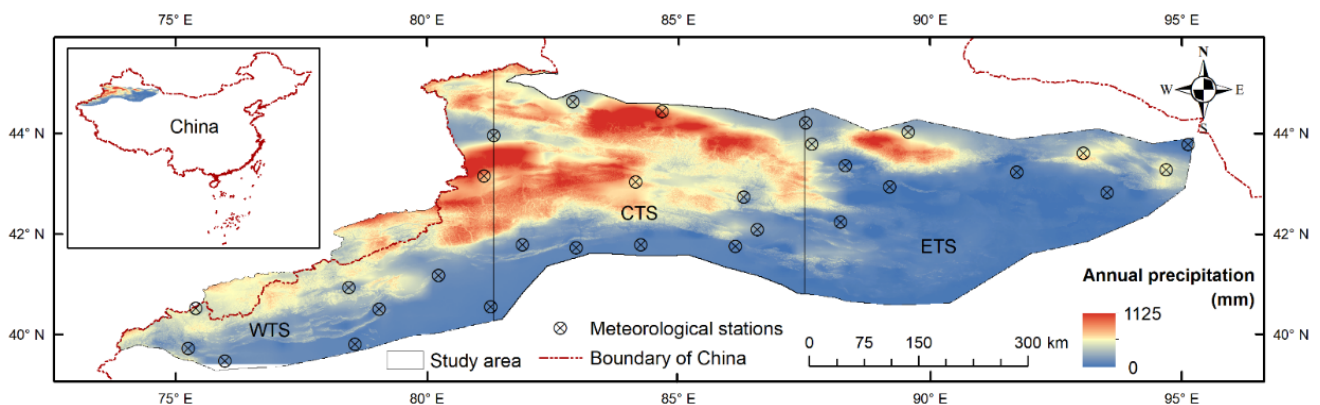


Figure 1. Location of the Tianshan Mountains and the spatial distribution of average annual precipitation from 1979 to 2020.

The precipitation is abundant in the Tianshan Mountains, with annual precipitation exceeding 300 mm (Figure 1). In the Tianshan Mountains, the northern slope has more precipitation than the southern slope. The CTS has the most precipitation (533 mm), followed by WTS and ETS. The Ili River Valley in WTS and the Bogda Mountains in CTS have abundant precipitation, and the Turpan-Hami basin in ETS and the plains in the southern Tianshan have the lowest precipitation (Figure 1). The main reason for this spatial distribution is the high altitude and the shape of Tianshan, that is, wide in the middle and narrow on both sides, which is beneficial to intercept and uplift the water vapor from the Atlantic and Arctic Oceans. The Ili River Valley, with a “pocket-shape”, is conducive to the accumulation of water vapor and the growth of vegetation [5].

2.2. Data

In this study, we used reanalysis products and observation data. First, we introduced DEM to downscaling ERA5 precipitation and then employed the observations of meteorological stations to verify the accuracy of downscaled data. Secondly, we used global temperature data and typical atmospheric circulation indexes to analyze the response of precipitation in Tianshan to global climate change.

2.2.1. ERA5 Precipitation Reanalysis Products

In this study, the ERA5 precipitation products were used as the source of precipitation downscaling. ERA5 is the fifth-generation reanalysis product of the European Centre for Medium-Range Weather Forecasts (<https://cds.climate.copernicus.eu/cdsapp#!/dataset/reanalysis-era5>, accessed on 17 January 2022). The time is from January 1979 to February 2021. The time resolution is one month, and the spatial resolution is $0.25^{\circ} \times 0.25^{\circ}$.

2.2.2. DEM

To downscale precipitation, we used the DEM from the United States Geological Survey (<http://srtm.csi.cgiar.org>, accessed on 17 January 2022), with a spatial resolution of 90×90 m. Based on the DEM, we extracted the aspect, slope, latitude, and longitude data using ArcGIS 10.4 software.

2.2.3. Observed Precipitation of Meteorological Stations

To evaluate the accuracy of downscaled precipitation, we used the observational precipitation data of 30 meteorological stations (See Table S1), which were provided by the National Meteorological Information Center (<http://data.cma.cn>, accessed on 17 January 2022). The time is from January 1979 to December 2020, and the time resolution is one month.

2.2.4. Berkeley Earth Land/Ocean Temperature

To analyze the response of precipitation in Tianshan to global warming, this study used the Berkeley Earth land/ocean temperature product (berkeleyearth.org). The time is from January 1850 to December 2020, and the time resolution is one month. It provides a global mean temperature record quite similar to records from Hadley's HadCRUT4, NASA's GISTEMP, NOAA's GlobalTemp, and Cowtan and Way and provides a spatially complete and homogeneous temperature field [66]. Two versions of the record are provided, treating areas with sea ice cover as either air temperature over sea ice or sea surface temperature under sea ice, and we used the former.

2.2.5. Atmospheric Circulation Index

The water vapor transportation system of Tianshan is mainly controlled by the westerly circulation and monsoon intensity. The water vapor mainly comes from the Atlantic Ocean, and a small amount of water vapor comes from the Arctic Ocean [67,68]. The Pacific Interdecadal Oscillation also affects the precipitation changes in Tianshan. Higher d-excess values (>10%), throughout the year, demonstrate that water vapor is intensively recycled in the Urumqi region [69]. Moreover, regional-scale hydrological conditions, including seasonal changes in moisture source, transport, and recycling in the Caspian/Aral Sea region may play a role through spatial and temporal d-variability [70]. In this study, eight representative atmospheric circulation indexes (Table 1) were used to analyze the response of precipitation in Tianshan to global climate change. The data were from the National Oceanic and Atmospheric Administration (<https://www.esrl.noaa.gov/psd/data/climateindices/list/>, accessed on 17 January 2022), with a time resolution of one month. For the introduction of indexes, please refer to Li et al. [71].

Table 1. Atmospheric circulation indexes used in this study.

Index	Abbreviation	Time
Arctic Oscillation	AO	from January 1979 to December 2020
Atlantic Multidecadal Oscillation	AMO	from January 1979 to December 2020
North Atlantic Oscillation	NAO	from January 1979 to December 2020
North Pacific pattern	NP	from January 1979 to June 2020
Pacific Interdecadal Oscillation	PDO	from January 1979 to December 2020
Tropical North Atlantic index	TNA	from January 1979 to December 2020
North Tropical Atlantic Sea Level Temperature index	NTA	from January 1979 to February 2020
Western Hemisphere warm pool	WHWP	from January 1979 to December 2020

2.3. Methods

First, we developed a GD-NLR downscaling model to simulate high-resolution monthly precipitation in Tianshan. Then, to quantify the significance and direction of precipitation trends, we used the Mann–Kendall trend test [72,73]. We are not only interested in whether a trend exists but also in its magnitude. For the quantification of the slope, we used the Thiel–Sen test [74,75]. Finally, we applied the Pearson correlation coefficient [76,77], cross-wavelet, and wavelet correlation methods to calculate the response of precipitation to global climate change.

2.3.1. Gradient Descent-Nonlinear Regression Downscaling Model

Topography and geographical location are the main factors affecting precipitation in mountainous areas [78]. Introducing terrain and geographic location to the downscaling of precipitation may be useful [79]. In this research, the slope, DEM, and aspect were used to show terrain, and latitude and longitude were used to show location. This research fitted nonlinear models for precipitation in 12 months and then trained the models using the GD algorithm [55]. The steps are as follows:

(1) First, resample the elevation, aspect and slope to a low resolution (LR) of $0.25^\circ \times 0.25^\circ$, and extract the latitude, and longitude of each pixel.

(2) Then, establish the nonlinear equations for monthly precipitation with elevation, aspect, slope, latitude, and longitude at LR, which can be expressed as follows:

$$P = F(A, E, Lon, Lat, S) + \Delta P, \quad (1)$$

where $F(A, E, Lon, Lat, S)$ represent the estimated precipitation; ΔP is residuals; A, E, Lon, Lat, S is aspect, elevation, longitude, latitude, and slope, respectively.

In the model, the cost function for regression is:

$$J(\theta) = \frac{1}{2m} \sum_{i=1}^m (h_{\theta}(x^{(i)}) - y^{(i)})^2, \quad (2)$$

where $x^{(i)}$ represents the feature of samples, $y^{(i)}$ is the target value, and m is the number of samples.

Then, we applied the GD algorithm to minimize the cost function, which was needed to find the partial derivative of $J(\theta)$:

$$\frac{\partial}{\partial \theta_j} J(\theta) = \frac{1}{m} \sum_{i=1}^m (h_{\theta}(x^{(i)}) - y^{(i)}) x_j^{(i)}, \quad (3)$$

The updating function of θ is:

$$\theta_j = \theta_j - \alpha \frac{1}{m} \sum_{i=1}^m (h_{\theta}(x^{(i)}) - y^{(i)}) x_j^{(i)}, \quad (4)$$

where α is the learning rate, and m is the number of samples. The time complexity of θ is $O(n)$. In each training, the data were randomly divided into a 70% training group and 30% test group. To improve the convergence speed, we scaled the feature samples as follows:

$$x^{(is)} = (x^{(i)} - x_{\min}) / (x_{\max} - x_{\min}), \quad (5)$$

(3) Calculate the residual ΔP_{LR} between the estimated precipitation $F(A, E, Lon, Lat, S)$ and ERA5 reanalysis P_{ERA5} at LR as Equation (6). Then, resample ΔP_{LR} to the high resolution of 90×90 m (HR) to obtain ΔP_{HR} using the bilinear interpolation method.

$$\Delta P_{LR} = P_{ERA5} - F(A, E, Lon, Lat, S), \quad (6)$$

(4) At HR, introducing $A_{HR}, E_{HR}, Lat_{HR}, Lon_{HR}$, and S_{HR} into the downscaling models of precipitation to obtain estimated precipitation P_{HR} . Then, summing the estimated precipitation P_{HR} and residual ΔP_{HR} to obtain the high-resolution precipitation P , as Equation (7), which finally achieves the downscaling of monthly precipitation.

$$P = P_{HR} + \Delta P_{HR}, \quad (7)$$

2.3.2. Cross-Wavelet Transform and Wavelet Correlation

The cross-wavelet transform and wavelet correlation methods are derived from Fourier transform. The wavelet depends on two parameters, that is, wavelet scale and time. For signal $x(t)$, its wavelet function $\varphi_{a,t}(t)$ can be expressed as follows:

$$\varphi_{a,t}(t) = \frac{1}{\sqrt{a}} \varphi\left(\frac{t - \tau}{a}\right), \quad (8)$$

Continuous wavelet transform is to apply a wavelet as a band-pass filter to a time series. For signal $x(t)$, the continuous wavelet transform can be defined as:

$$W_x(a, \tau) = \frac{1}{\sqrt{a}} \int_{-\infty}^{+\infty} x(t) \varphi^*\left(\frac{t - \tau}{a}\right) dt = \int_{-\infty}^{+\infty} x(t) \varphi_{a,t}^*(t) dt, \quad (9)$$

where $*$ represents the complex conjugate form, $W_x(a, \tau)$ represents wavelet scale, that is, the contribution of a to signal $x(t)$.

The cross-wavelet transform between two signals $x(t)$ and $y(t)$ is defined as $W^{XY} = W^X W^Y*$. The energy of cross-wavelet is defined as $|W^{XY}|$. The wavelet correlation is to calculate the statistical relationship between $x(t)$ and $y(t)$ in time-frequency space, which is defined as follows:

$$R_{x,y}^2(s) = \frac{|S(s^{-1} W_t^{XY}(s))|^2}{S(s^{-1} |W_t^X(s)|^2) \cdot S(s^{-1} |W_t^Y(s)|^2)}, \quad (10)$$

where S is the smoothing operator. s is the circular standard deviation, that is, $\sqrt{-2 \ln(R/n)}$, $R = \sqrt{X^2 + Y^2}$.

Another statistic produced by cross-wavelet transform is the cross-wavelet phase angle $\varphi_{x,y}$, which can describe the potential lead-lag relationship between two signals, and it can be calculated as:

$$\varphi_{x,y} = \arctan\left(\frac{I\{S(s^{-1} W^{XY}(s))\}}{R\{S(s^{-1} W^{XY}(s))\}}\right), \quad \varphi_{x,y} \in [-\pi, \pi], \quad (11)$$

where I represents the part where the wavelet function φ matches the original signal well, and R represents the part where the two match weakly. The significance test of wavelet correlation is calculated by the Monte Carlo method.

3. Results

3.1. Accuracy of the Downscaled Dataset

Based on the GD algorithm, we obtained the downscaled equations of monthly precipitation (see Table S2). In twelve months, there are strong nonlinear relationships of precipitation with elevation, aspect, slope, latitude, and longitude. According to Table S2, the dependence of precipitation on each factor from high to low is latitude, altitude, longitude, aspect, and slope. To further assess the dependence of precipitation on different factors, we removed elevation, aspect, slope, longitude, and latitude from models, respectively, and analyzed the changes in model accuracy (Table 2). When the latitude, longitude, elevation, aspect, and slope were removed from the model, the R^2 between simulations and targets becomes 0.30–0.43, 0.38–0.50, 0.42–0.53, 0.44–0.57, and 0.48–0.69, respectively. If we just consider latitude, longitude, and elevation, the R^2 between simulations and targets will become 0.35–0.48. Overall, the precipitation in the Tianshan Mountains has the highest dependence on latitude and longitude, followed by elevation, which indicates that geographical location and topography have important influences on the precipitation distribution in the Tianshan Mountains.

Table 2. Accuracy test (R^2) of GD-NLR models.

Month	GD							Least Square
	GD-NLR	without Latitude	without Aspect and Slope	without Longitude	without Slope	without Aspect	without Elevation	
1	0.73	0.37	0.42	0.40	0.59	0.48	0.45	0.64
2	0.78	0.39	0.48	0.44	0.69	0.53	0.49	0.62
3	0.79	0.38	0.37	0.40	0.58	0.50	0.45	0.72
4	0.78	0.30	0.40	0.48	0.50	0.49	0.45	0.54
5	0.75	0.43	0.39	0.50	0.59	0.57	0.53	0.62
6	0.69	0.40	0.36	0.41	0.50	0.46	0.45	0.65
7	0.66	0.39	0.35	0.42	0.48	0.44	0.42	0.63
8	0.70	0.43	0.40	0.49	0.58	0.53	0.51	0.59
9	0.73	0.34	0.41	0.38	0.49	0.48	0.42	0.60
10	0.73	0.32	0.38	0.38	0.53	0.49	0.43	0.60
11	0.73	0.40	0.44	0.47	0.58	0.55	0.50	0.71
12	0.75	0.41	0.47	0.45	0.62	0.52	0.49	0.59

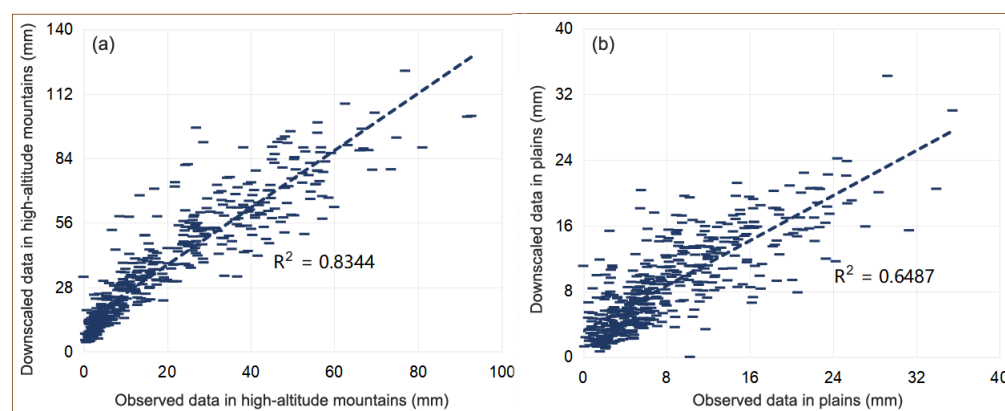
To verify the applicability of the GD-NLR models, we calculated the coefficient of determination (R^2) between model outputs and target values in the test period. Table 2 shows that the GD-NLR model performs well in each month, with R^2 above 0.65 in the testing period. To further verify the accuracy of the GD-NLR models, we also trained the model using the least squares method. Table 2 shows that the accuracy of the GD-NLR model is significantly better than that of the least square model. The R^2 is 0.66–0.79 between targets and the simulations by the GD-NLR model, and that is 0.54–0.72 between targets and the simulations by least square model. Overall, the GD-NLR model has high accuracy and can be applied to simulate the precipitation changes in the Tianshan Mountains.

Based on the GD-NLR model, we obtained the high-resolution (90×90 m) monthly precipitation dataset in the Tianshan Mountains. Due to the high altitude and complex terrain, there are only 30 meteorological stations in the study area. We verified the accuracy of the downscaling dataset by the observed data from 30 stations (Table 3). At the 30 stations, the slope between the downscaled and observed precipitation is close to 1, the NSE is above 0.50, and the MAE and RMSE are below 15 mm. At stations such as Zhaosu and Caijiahu, the NSE between the simulated and observed precipitation is higher than 0.80, and the MAE and RMSE are lower than 10 mm.

Table 3. Accuracy test of downscaled dataset.

Station	Slope	MAE	RMSE	NSE
Kashgar	1.53	14.43	14.35	0.61
Akqi	1.22	5.79	2.31	0.60
Wuqia	0.66	8.88	12.57	0.55
Turgart	1.05	6.34	3.08	0.83
Bachu	0.92	10.56	13.97	0.71
Kalpin	0.56	12.80	7.49	0.64
Zhaosu	0.53	3.97	8.35	0.52
Baluntai	0.57	2.37	4.30	0.51
Byanbulak	0.65	3.40	5.89	0.51
Yining	1.00	6.96	2.72	0.68
Yanqi	1.10	9.97	14.38	0.72
Aksu	0.90	6.83	9.75	0.59
Baicheng	0.56	6.26	9.96	0.52
Kuqa	0.65	4.79	7.67	0.51
Korla	0.70	4.15	6.67	0.52
Alar	0.84	6.52	9.62	0.51
Wusu	0.70	13.14	9.57	0.53
Luntai	0.75	4.37	7.61	0.51
Jinghe	0.82	6.29	9.91	0.66
Barkol	0.73	3.44	6.22	0.52
Yiwu	1.03	15.42	11.99	0.61
Urumqi	0.79	1.59	2.74	0.63
Dabancheng	0.90	1.71	2.67	0.50
Shisanjianfang	0.80	4.25	3.24	0.57
Qitai	0.60	9.42	14.38	0.51
Kumux	0.99	7.60	9.97	0.85
Naomao Lake	0.56	4.59	7.64	0.51
Turpan	0.91	6.51	10.81	0.65
Caijiahu	1.28	3.20	5.77	0.61
Hami	0.65	2.35	3.99	0.51

To further verify the downscaling dataset, we plotted scatter plots of downscaled and observed data of eight stations in high-altitude and 22 stations in plains (see Table S1). Figure 2 shows that the downscaled dataset has high accuracy in both high-altitude and plain areas. The R^2 between the downscaled and observed data is 0.83 in high altitude mountains, and that is 0.65 in plains. In addition, the downscaled precipitation is slightly higher than observed precipitation, and this is more pronounced in high-altitude mountains.

**Figure 2.** Accuracy of the downscaled dataset in high-altitude mountains (a) and plains (b).

To assess the improvement of downscaling, we compared the accuracy before and after downscaling. Table 4 indicates that the accuracy of the downscaled dataset is better than the ERA5 reanalysis in both high-altitude mountains and plains. In high-altitude mountains, the slope of downscaled data and observations is 1.24, the NSE is 0.83, and MAE

and RMSE are both lower than 9 mm, while the Slope of ERA5 reanalysis and observations is 1.47, the NSE is 0.61, and MAE and RMSE are both higher than 9 mm. In plains, the slope of downscaled data and observations is 1.16, the NSE is 0.65, and MAE and RMSE are both lower than 9 mm, while the slope of ERA5 reanalysis and observations is 1.33, the NSE is 0.49, and MAE and RMSE are both higher than 9.5 mm. The above results indicate that there is a significant improvement in downscaling.

Table 4. Accuracy comparison of downscaled dataset and ERA5 reanalysis.

Area	Data	Slope	NSE	MAE	RMSE
High-altitude mountains	Downscaled data	1.24	0.83	7.73	8.04
	ERA5 reanalysis	1.47	0.61	9.05	11.23
Plains	Downscaled data	1.16	0.65	7.05	8.80
	ERA5 reanalysis	1.33	0.49	9.72	12.89

To further assess the improvement in downscaling, we partly extracted the downscaled precipitation in July and compared it with the ERA5 reanalysis and observations for the corresponding time (Figure 3). Compared with the observations and ERA5 reanalysis, the spatial resolution of the downscaled data has been significantly improved, which can show the spatial distribution of precipitation in the Tianshan Mountains more clearly. Overall, the downscaled dataset has high accuracy and can accurately reveal the precipitation change in the Tianshan Mountains.

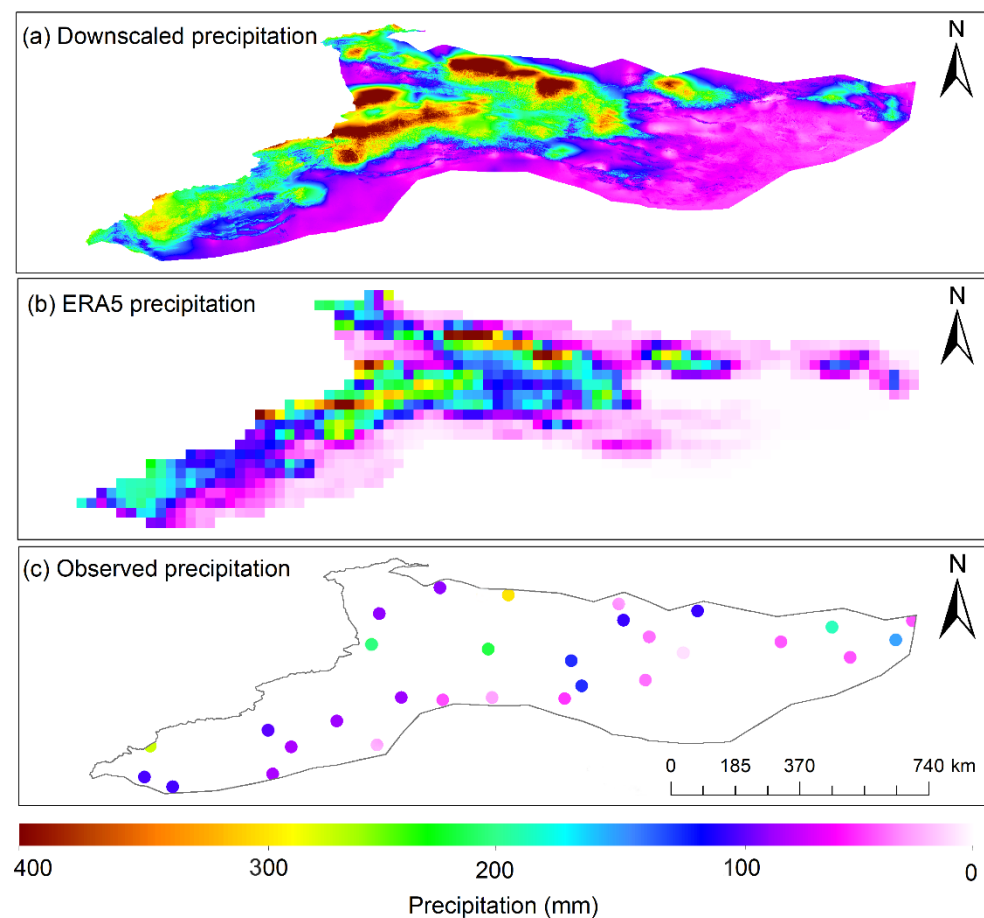


Figure 3. The comparison of downscaled dataset (a), ERA5 reanalysis (b), and observations (c): average precipitation in July from 1979 to 2020.

3.2. Temporal and Spatial Changes of Precipitation

We obtained the annual precipitation by summing the precipitation from March to the following February. Table 5 shows the descriptive statistics and trend test results of annual precipitation. The annual precipitation in Tianshan is 368 mm. The CTS has the most abundant precipitation at 533 mm, followed by WTS with 405 mm, and ETS at 175 mm. From 1979 to 2020, the Tianshan showed a wetting trend with a rate of 26.4 mm/10a ($Z = 1.42$, $\alpha = 0.10$). The precipitation in WTS has the fastest increase at 34.1 mm/10a, followed by CTS and ETS, with increasing rates of 10.3 and 4 mm/10a, respectively. The Sen slope verifies the changing trend of precipitation. The SD and CV values indicate a large inter-annual difference of precipitation in WTS.

Table 5. Descriptive statistics and trend tests for annual precipitation.

	Descriptive Statistics					Mann–Kendall Trend Test	Sen's Slope
	N	Mean (mm)	SD	CV (%)	Slope (mm/a)	Z	
Tianshan	41	368.09	32.53	8.84	2.64	1.42 *	2.61
WTS	41	405.26	45.11	11.13	3.41	0.60	3.44
CTS	41	532.55	45.87	8.61	1.03	0.79	1.03
ETS	41	174.55	24.11	13.82	0.40	1.26 *	0.41

* indicates that the slope has passed the significance test of 0.10.

From 1979 to 2020, the precipitation in Tianshan showed an increasing trend, at a rate of 26 mm/10a (Figure 4). The precipitation in the WTS increased the fastest, followed by CTS and ETS. The Aksu River Basin, located in WTS, has the most obvious increase in precipitation, while the precipitation in the northern part of CTS and ETS showed a decreasing trend.

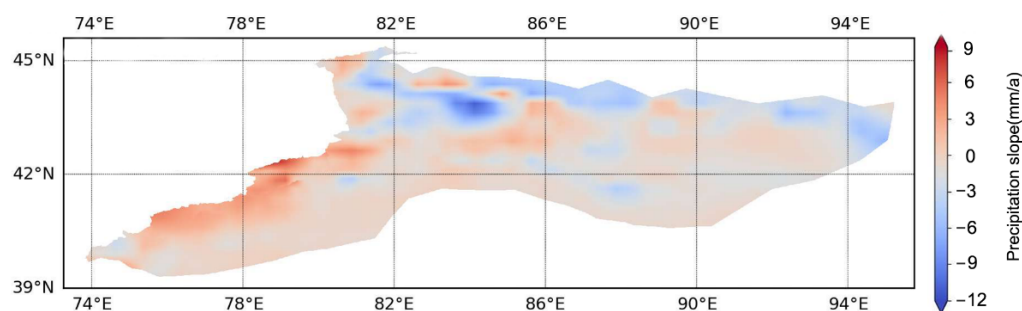


Figure 4. Spatial changes of the slope of annual precipitation in the Tianshan Mountains.

3.3. Response of Precipitation to Global Warming

Figure 5 indicates that, since 1850, the world has shown a warming trend, and the trend has accelerated after 1910, which has been confirmed by lots of studies [66,80]. Scholars have reached some consensus on the causes of global warming. One is the change in the natural laws of the climate system, that is, the result of natural change [81], and the other is that human activities have increased the rate of natural change [82,83].

In recent years, with global warming, the global average precipitation has shown an increasing trend [2]. How does the precipitation in Tianshan respond to global warming? Figure 6 shows the scatter plots between precipitation and global temperature on a monthly scale. In Tianshan, the correlation coefficient between precipitation and global temperature is 0.88, indicating that the precipitation in Tianshan is sensitive to global warming. The CTS has the highest elevation and the most precipitation, and it is more sensitive to global warming than WTS and ETS. In WTS, CTS, and ETS, the correlation coefficient between precipitation and global temperature is 0.86, 0.87, and 0.78, respectively. Moreover, we also

calculated the correlation coefficient between precipitation and local temperature, and the results are shown in Figure S1. In WTS, CTS and ETS, the correlation coefficients between precipitation and local temperature are 0.84, 0.87, and 0.78, respectively, which are close to that of global temperature. The above results indicate that the precipitation in the Tianshan Mountains is sensitive to warming. The formation mechanism of regional precipitation is complex. There are many properties of convection that can change as the atmosphere warms, including the effective water-vapor gradient, cloud pressure depth, and cloud velocity [84]. The response mechanism of the precipitation in the Tianshan Mountains to global warming needs further study.

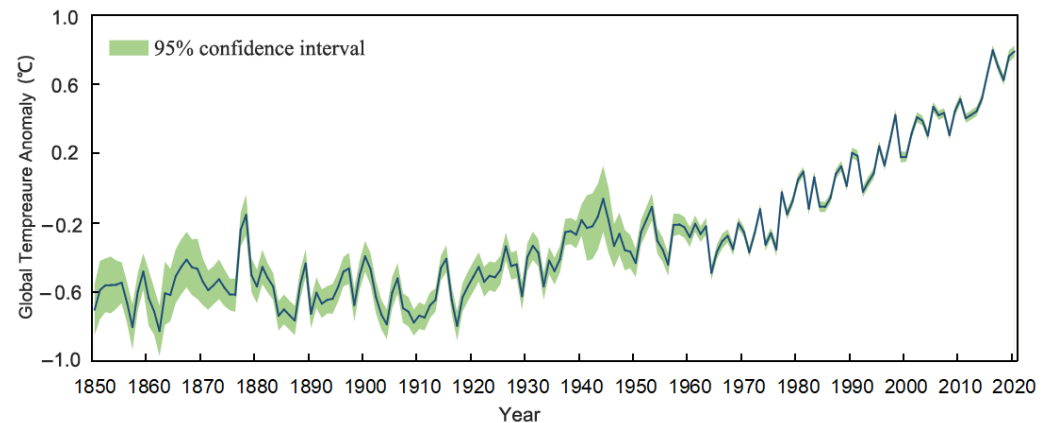


Figure 5. Global average surface temperature anomaly from 1850 to 2020 (relative to the average value from 1970 to 2000).

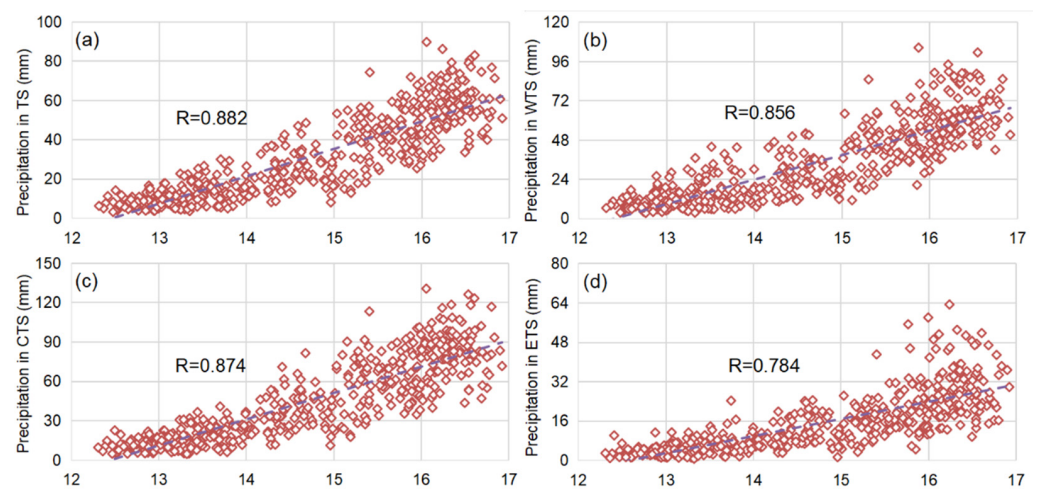


Figure 6. Scatter plots between monthly precipitation and global surface temperature: (a) Tianshan, (b) WTS, (c) CTS, and (d) ETS.

Figure 7 shows the cross-wavelet and wavelet correlations between global temperature and the precipitation in Tianshan. During the entire study period (1979–2020), precipitation and global temperature have a significant resonance period of 8–15 months, with the correlation coefficient above 0.9, and the correlation is stable. This illustrates that on a scale of 8–15 months, the precipitation in Tianshan is very sensitive to global warming.

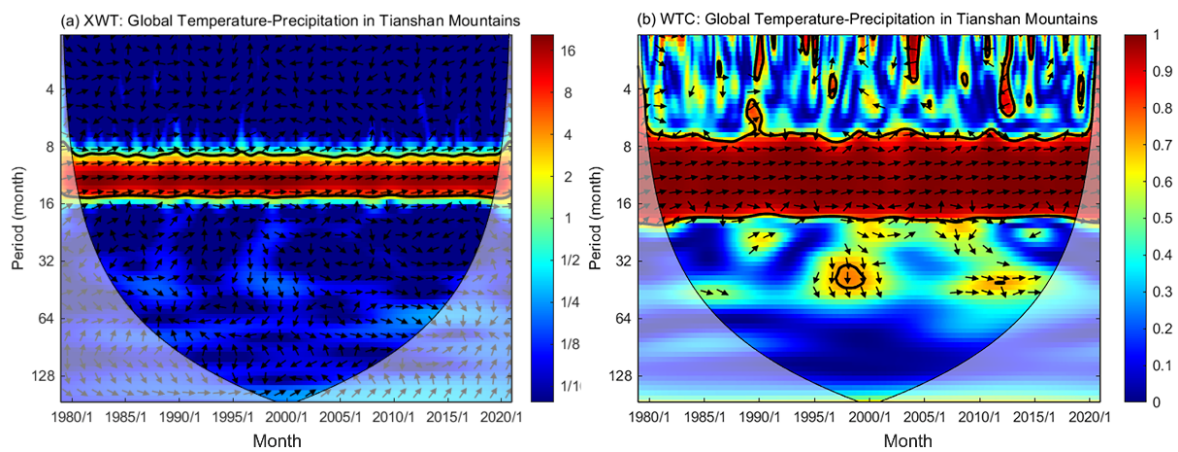


Figure 7. Cross-wavelet (a) and wavelet correlation (b) between global surface temperature and precipitation in Tianshan.

3.4. Response of Precipitation to Circulation Changes

The atmospheric circulation index can characterize climate change on a regional scale. During the study period, eight circulation indexes fluctuate cyclically (see Figure S2). On the whole, AMO, TNA, NTA, and WHWP show an upward trend, PDO shows a downward trend, and AO, NAO, and NP have small changes, with a linear trend close to zero. From the perspective of stability, the changes of AO, NAO and NP are relatively unstable, with obvious differences between different months.

The Pearson correlation coefficient was used to calculate the correlations between precipitation and eight atmospheric circulation indexes, and the results are shown in Figure 8. On the monthly scale, AMO, NP, PDO, and WHWP have positive impacts on precipitation in Tianshan. The correlation coefficient between precipitation and NP is the highest, above 0.60, followed by WHWP and AMO, at about 0.20, indicating that NP, WHWP, and AMO are the main circulation factors affecting the precipitation changes in Tianshan. Different regions respond differently to circulation changes. In WTS, NAO has a negative impact on precipitation, and AMO, NP, PDO, TNA and WHWP have positive impacts on precipitation changes. While in CTS and ETS, the precipitation changes are mainly determined by AMO, NP, PDO, and WHWP.

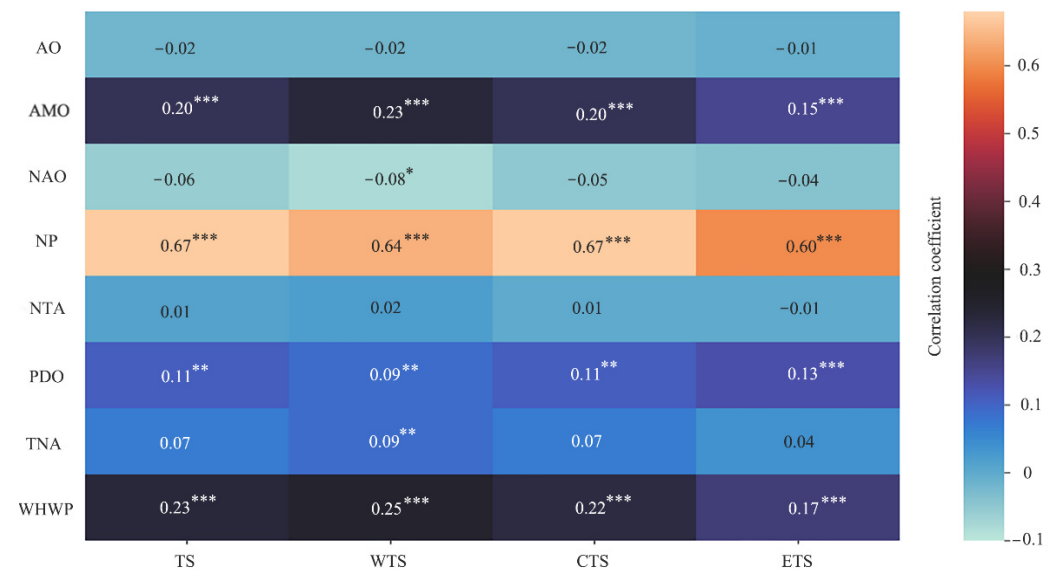


Figure 8. Correlation coefficients between monthly precipitation and atmospheric circulation indexes: ^{***}, ^{**}, and ^{*} represent significance at the levels of 1%, 5%, and 10%, respectively.

In different seasons, there are significant differences in the correlation between precipitation and atmospheric circulation (Figure 9). In spring, AMO, NTA, PDO, TNA, and WHWP have positive impacts on precipitation changes, while NP has a negative impact on precipitation changes in Tianshan. Among the eight indexes, PDO has the greatest impact on precipitation, with a correlation coefficient of 0.52, followed by NP, with a correlation coefficient of -0.43 . In WTS, precipitation changes are mainly determined by NP and PDO. In CTS, precipitation changes are mainly determined by NP, NTA, PDO, TNA and WHWP. While in ETS, precipitation changes are mainly determined by AMO, NTA, PDO, TNA, and WHWP. In summer, NAO, NP, and PDO have positive impacts on precipitation changes. The precipitation in WTS is mainly determined by NP, and the correlation coefficient is 0.31, while the precipitation in ETS is mainly determined by NAO and PDO. In autumn, AMO have a negative impact on precipitation changes in the ETS. In addition, NP and TNA have negative impacts on precipitation changes, but the impact is not significant. In winter, AO has a negative impact on precipitation changes in the CTS. In addition, NAO is negatively correlated with precipitation, and TNA is positively correlated with precipitation, with a correlation coefficient of about 0.20, but they both failed the significance test.

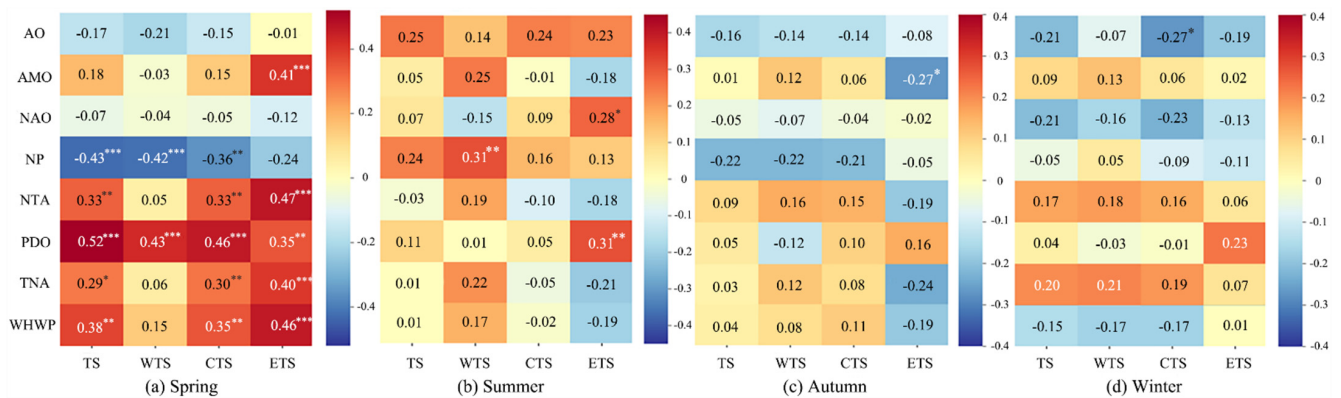


Figure 9. Correlation coefficients between precipitation and atmospheric circulation indexes in spring (a), summer (b), autumn (c), and winter (d): ***, **, and * represent significance at the level of 1%, 5%, and 10%, respectively.

Cross-wavelet transform and wavelet correlations can reveal the response on different time scales and the lag time of precipitation relative to circulation changes. Figure 10 shows the cross-wavelet and wavelet correlations between precipitation with AO, AMO, NAO, and NP. During 1990–1992, precipitation and AO had a resonance period of 10–16 months, and they showed a significant negative correlation. During 1985–1989, precipitation and AO had a secondary resonance of 30–36 months, and precipitation change lagged AO by an average of 495 days (Figure 10a,b). In the period of 1–8 months, precipitation and AMO present a discontinuous negative correlation. In 1985–1990, 1994–2000, and 2002–2017, precipitation and AMO had a resonance period of 8–16 years, and they showed a significant positive correlation. In 1993–2000 and 2003–2015, there was a resonance period of 3–5 years between precipitation and AMO (Figure 10c,d). In 1980, 1986–1987, 1995, 1997, 2007–2012, and 2015, there was a significant resonance period of 1–8 months between precipitation and NAO, but the correlation was unstable and gradually changed from a positive correlation to a negative correlation over time. In 1985–1987, there was a significant resonance period of 32–36 months, and the precipitation changes lagged NAO by an average of 510 days. In 2000, there was a four-year resonance period between precipitation and NAO, and NAO lagged the precipitation changes by an average of 360 days (Figure 10e,f). During the entire study period, precipitation and NP had a common cycle of 8–17 months, with a significant positive correlation, indicating that NP was an important circulation factor affecting the changes in precipitation in Tianshan. Precipitation and NP had a common cycle of 2–8 years, and NP lagged the precipitation changes by an average of 456 days. In addition, there is a

discontinuous correlation between precipitation and NP on the scale of 1–8 months, while the correlation is not stable and varies obviously in different years (Figure 10g,h).

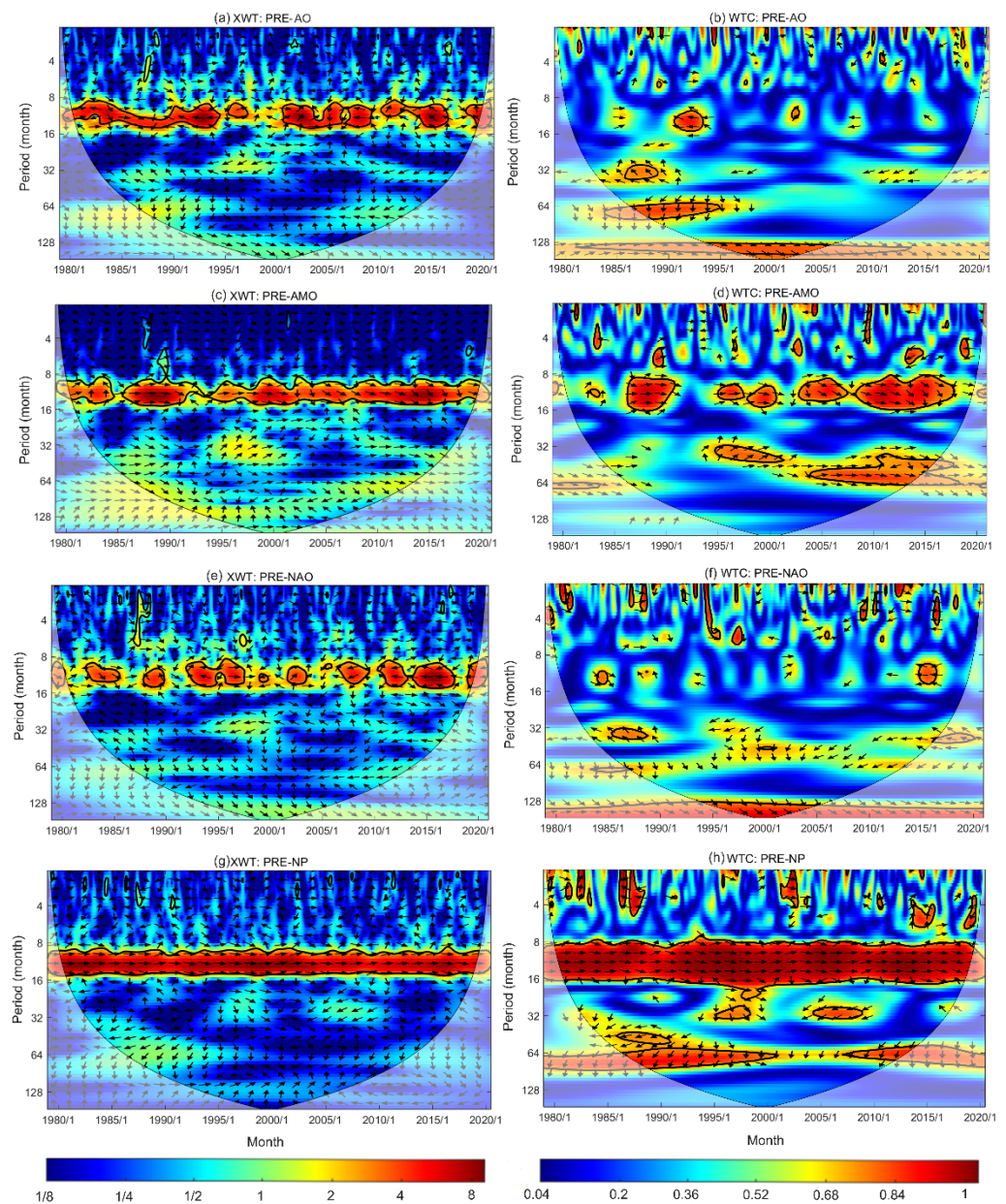


Figure 10. Cross-wavelet and wavelet correlations between precipitation and AO, AMO, NAO, and NP: (a,c,e,g) are cross-wavelet analyses between precipitation and AAO, AMO, NAO, and NP, respectively. (b,d,f,h) are wavelet correlations between precipitation and AO, AMO, NAO, and NP, respectively.

Figure 11 shows the cross-wavelet and wavelet correlations between precipitation with NTA, PDO, TNA, and WHWP. In 1983, 1987, 2000, and 2004, precipitation and NTA had a common cycle of 1–8 months, and precipitation changes lagged NTA by an average of 17 days. In 1980–1982, 1986, 2001–2004 and 2011–2017, precipitation and NTA had a common cycle of 8–16 months, and the correlation was unstable. In 1992–2004, precipitation and NTA had a common cycle of 2–4 years, and precipitation changes lagged NTA by an average of 137 days (Figure 11a,b). In 1985, 1989, 1995, 2000–2008, and 2015, precipitation and PDO had a common cycle of 1–8 months, and they gradually changed from a negative correlation to a positive correlation over time. In 1987–2000, 2005 and 2009–2017, precipitation and PDO had a common cycle of 8–16 months, and precipitation

changes lagged PDO by an average of 30 days. In 2000–2012, precipitation and PDO had a common cycle of 5 years, and precipitation changes lagged PDO by an average of 228 days (Figure 11c,d). In 1993, 2008, 2011 and 2017, precipitation and TNA had a resonance period of 1–8 months, showing a negative correlation. In 1986–1992, 2003–2005, and 2008–2017, precipitation and TNA had a significant resonance period of 8–16 months. In 1993–2005, there was a significant resonance period of 2–5 years between precipitation and TNA, and precipitation changes lagged TNA by an average of 160 days (Figure 11e,f). In the cycle of 1–8 months, precipitation and WHWP show a discontinuous negative correlation. In 1982–1985, 1990–1992, and 1995–2019, precipitation and WHWP had a significant resonance period of 8–16 months, and TNA lagged the precipitation changes by an average of 45 days. In 1995–2015, precipitation and WHWP had a common cycle of 2–5 years, and precipitation changes lagged WHWP by an average of 160 days (Figure 11g,h).

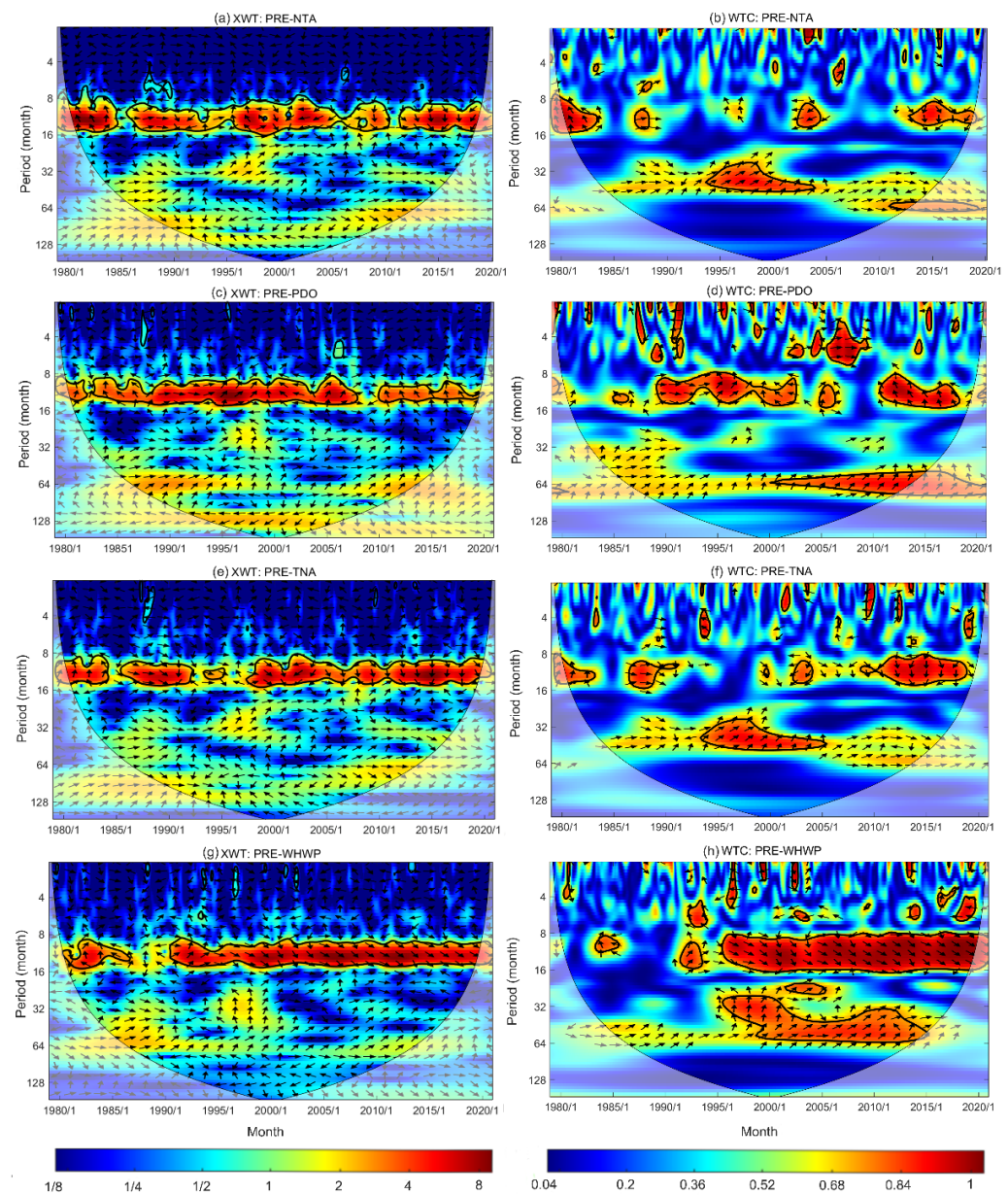


Figure 11. Cross-wavelet and wavelet correlations between precipitation and NTA, PDO, TNA, WHWP: (a,c,e,g) are cross-wavelet analyses between precipitation and NTA, PDO, TNA, and WHWP, respectively. (b,d,f,h) are wavelet correlations between precipitation and NTA, PDO, TNA, and WHWP, respectively.

4. Discussion

Global climate change has an important impact on regional precipitation changes, and this study confirmed it. We found that in the context of global warming, Tianshan showed a wetting trend with a rate of 26.4 mm/10a from 1979 to 2020. The climate change in Central Asia is related to the change of the westerly zone and monsoon intensity [68,85,86]. This study indicated that NAO and AMO have an important influence on precipitation changes in Tianshan. In the years when NAO is strong, the intensity of the subtropical high in the western Pacific is significantly weakened, and the Aleutian Low is relatively strong, corresponding to the weakening of the Siberian High [23]. When NAO is in a positive phase, there will be abnormal cyclones in the mid-high latitudes of the North Atlantic [87], and the enhanced westerly wind will bring the warm and humid North Atlantic water vapor from the ocean to Eurasia. In addition, NAO can influence the climate of East Asia through atmospheric teleconnection and abnormal planetary waves [22,88,89]. There are two views for AMO affecting the climate of East Asia: one is that AMO causes air-sea feedback in the western Pacific [90], and the other is that AMO affects the atmospheric circulation and then causes changes in the tropospheric temperature of Eurasia [91]. The orthophase of AMO is conducive to enhancing the summer monsoon of East Asia [90,91]. Studies have shown that AO is related to westerly jet, Siberian high and Rossby wave activities, and it has an important impact on climate change in Eurasia [92–94]. AO affects the Siberian High and thus the strength of the winter monsoon [95]. In addition, AO affects the mid and high latitude atmospheric circulation system including the upper trough and the westerly jet, which in turn affects the occurrence of cold waves [96]. When AO is in the negative phase, the winter monsoon in East Asia is strong, and the intensity and duration of the cold wave are greater than that of the positive phase. The heterogeneous relationship of vortex temperature changes between Asia and the North Pacific is related to the heterogeneous relationship of atmospheric heating [97,98]. This study shows that NP and PDO have an important impact on precipitation changes in Tianshan. Arctic warming has an impact on climate change in Eurasia [99,100], and PDO is one of the main drivers of Arctic warming [101]. The positive phase of PDO may cause the East Asian trough to deepen [102], and the growth of the East Asian trough may cause the temperature to decrease in East Asia [22,103]. In addition, the enhancement of PDO will produce a westerly component, which may increase the prevailing westerly jets in mid-latitudes [104,105] and increase the cold northerly winds in Asia and Eastern Europe [67,106]. Since 2004, the enhancement of PDO has contributed 54% to the fall of autumn temperature in Eurasia [71]. This study shows that the response of regional precipitation to circulation changes has a hysteresis. Compared with the atmosphere, the ocean changes more slowly in the climate system. Atmospheric circulation may cause anomalies in the underlying layer of snow, sea ice and sea temperature. These anomalies may last for a period of time, which creates conditions for later changes in regional precipitation [107–109].

Based on global temperature data and eight atmospheric circulation indexes, we analyzed the response of precipitation in Tianshan to global climate change. We know that changes in the climate system are the result of a combination of different factors. For example, there is a connection between snow and atmosphere. Climate forcing leads to the changes of snow cover in the northern hemisphere [110], which in turn affects the phase and amplitude of atmospheric circulations [111,112]. However, there are still many challenges in understanding the snow–atmosphere coupling, and the complex physical mechanisms related to precipitation changes in Tianshan need to be further studied.

In this study, a GD-NLR model was developed to downscale the precipitation in alpine mountains, which provides a new idea for simulating high-resolution precipitation in mountainous areas. Due to the high altitude and complex terrain, there are only 30 meteorological stations that could be used to verify the accuracy of downscaling precipitation. We will explore other methods to further evaluate the accuracy of downscaled datasets in the future, such as comparing the dataset with other precipitation products and downscaled results. Moreover, despite numerous studies experimenting with a wide

range of models for statistical downscaling, none have clearly outperformed others [52]. For the arid Tianshan Mountains, further improvements and customization of traditional regressions and machine learning methods are needed to provide more credible simulations of precipitation. Future work may introduce multiple machine learning algorithms to improve each step of downscaling to improve overall performance.

5. Conclusions

The main contribution of this study is to provide a high-resolution (90×90 m) precipitation dataset in Tianshan and confirms that global warming, the North Pacific pattern, the Western Hemisphere warm pool, and the Atlantic Multidecadal Oscillation are related to the humidification of Tianshan over the past 40 years. The precipitation in Tianshan and global temperature have a resonance period of 8–15 months, and the correlation coefficient is above 0.9. In Tianshan, spring precipitation is determined mainly by the Atlantic Multidecadal Oscillation, North Tropical Atlantic Sea Level Temperature, Pacific Interdecadal Oscillation, Tropical North Atlantic Index, Western Hemisphere warm pool, North Pacific pattern, summer by North Pacific pattern, North Atlantic Oscillation, and Pacific Interdecadal Oscillation, autumn by Atlantic Multidecadal Oscillation, and winter by Arctic Oscillation. The insights gained in this study may help to understand the regional precipitation response to global change.

This study simulated precipitation changes by downscaling ERA5 products. It is worth noting that there are certain uncertainties in reanalysis products; therefore, the data need to be further evaluated when applied to other regions. Numerous studies have shown that vegetation has an impact on precipitation change. Due to a lack of vegetation data with high spatial and temporal resolution, this study only introduced topography, latitude, and longitude in precipitation downscaling. If the required data are available, the research can be continued further.

The present study lays the groundwork for future research into the precipitation forecast, which is of great significance to water resources management in Tianshan. Based on future climate scenarios, water management planning should be oriented to generate new strategies to cope with possible future droughts and floods.

Supplementary Materials: The following supporting information can be downloaded at: <https://www.mdpi.com/article/10.3390/rs14030519/s1>, Table S1: Location of 30 meteorological stations; Table S2: Parameters of the downscaling models; Figure S1: Scatter plots between monthly precipitation and local temperature: (a) Tianshan, (b) WTS, (c) CTS, and (d) ETS; Figure S2: Changes in atmospheric circulation indexes: (a) AO, (b) NAO, (c) NP, (d) PDO, (e) AMO, (f) TNA, (g) NTA, and (h) WHWP.

Author Contributions: Conceptualization, M.F. and J.X.; methodology, M.F. and J.X.; formal analysis, investigation and data curation, J.X.; writing—original draft preparation, M.F.; writing—review and editing, D.L. and Y.C.; supervision, J.X., D.L. and Y.C. All authors have read and agreed to the published version of the manuscript.

Funding: The research is supported by the National Natural Science Foundation of China (Grant No. U1903208, 41871025).

Institutional Review Board Statement: Not applicable.

Data Availability Statement: The data used in this study are available from Mengtian Fan (52193901013@stu.ecnu.edu.cn).

Acknowledgments: We thank the State Key Laboratory of Desert and Oasis Ecology, Xinjiang Institute of Ecology and Geography, Chinese Academy of Sciences. We also thank the editors and three reviewers for their constructive comments and suggestions on the manuscript.

Conflicts of Interest: The authors declare that they have no known competing financial interest or personal relationship.

References

1. IPCC. *Climate Change 2021: The Physical Science Basis: Contribution of Working Group I to the Sixth Assessment Report of the Intergovernmental Panel on Climate Change*; Cambridge University Press: Cambridge, UK, 2021.
2. Salzmänn, M. Global warming without global mean precipitation increase? *Sci. Adv.* **2016**, *2*, e1501572. [[CrossRef](#)]
3. Wentz, F.J.; Ricciardulli, L.; Hilburn, K.; Mears, C. How much more rain will global warming bring? *Science* **2007**, *317*, 233–235. [[CrossRef](#)] [[PubMed](#)]
4. Sun, J.Q.; Ao, J. Changes in precipitation and extreme precipitation in a warming environment in China. *Chin. Sci. Bull.* **2013**, *58*, 1395–1401. [[CrossRef](#)]
5. Fan, M.T.; Xu, J.H.; Chen, Y.N.; Li, W.H. Simulating the precipitation in the data scarce Tianshan Mountains, Northwest China based on the Earth system data products. *Arab. J. Geosci.* **2020**, *13*, 637. [[CrossRef](#)]
6. Hu, X.L.; Yuan, W.H. Evaluation of ERA5 precipitation over the eastern periphery of the Tibetan plateau from the perspective of regional rainfall events. *Int. J. Climatol.* **2021**, *41*, 2625–2637. [[CrossRef](#)]
7. Dong, Q.; Wang, W.G.; Kunkel, K.E.; Shao, Q.X.; Xing, W.Q.; Wei, J. Heterogeneous response of global precipitation concentration to global warming. *Int. J. Climatol.* **2021**, *41*, E2347–E2359. [[CrossRef](#)]
8. Zhang, Y.N.; Liang, C. Author Correction: Analysis of Annual and Seasonal Precipitation Variation in the Qinba Mountain area, China. *Sci. Rep.* **2021**, *11*, 24387. [[CrossRef](#)] [[PubMed](#)]
9. Li, B.F.; Chen, Y.N.; Chen, Z.S.; Xiong, H.G.; Lian, L.S. Why does precipitation in northwest China show a significant increasing trend from 1960 to 2010? *Atmos. Res.* **2016**, *167*, 275–284. [[CrossRef](#)]
10. Allan, R.P.; Soden, B.J.; John, V.O.; Ingram, W.; Good, P. Current changes in tropical precipitation. *Environ. Res. Lett.* **2010**, *5*, 025205. [[CrossRef](#)]
11. Chou, C.; Chiang, J.C.H.; Lan, C.W.; Chung, C.H.; Liao, Y.C.; Lee, C.J. Increase in the range between wet and dry season precipitation. *Nat. Geosci.* **2013**, *6*, 263–267. [[CrossRef](#)]
12. Dwyer, J.G.; Biasutti, M.; Sobel, A.H. The effect of greenhouse gas-induced changes in SST on the annual cycle of zonal mean tropical precipitation. *J. Clim.* **2014**, *27*, 4544–4565. [[CrossRef](#)]
13. Espinoza, J.C.; Ronchail, J.; Marengo, J.A.; Segura, H. Contrasting North–South changes in Amazon wet-day and dry-day frequency and related atmospheric features (1981–2017). *Clim. Dyn.* **2019**, *52*, 5413–5430. [[CrossRef](#)]
14. Wehner, M.F. Predicted twenty-first-century changes in seasonal extreme precipitation events in the parallel climate model. *J. Clim.* **2004**, *17*, 4281–4290. [[CrossRef](#)]
15. Goswami, B.N.; Venugopal, V.; Sengupta, D.; Madhusoodanan, M.S.; Xavier, P.K. Increasing trend of extreme rain events over India in a warming environment. *Science* **2006**, *314*, 1442–1445. [[CrossRef](#)]
16. Fischer, E.M.; Beyerle, U.; Knutti, R. Robust spatially aggregated projections of climate extremes. *Nat. Clim. Chang.* **2013**, *3*, 1033–1038. [[CrossRef](#)]
17. Kharin, V.V.; Zwiers, F.W.; Zhang, X.; Wehner, M. Changes in temperature and precipitation extremes in the CMIP5 ensemble. *Clim. Chang.* **2013**, *119*, 345–357. [[CrossRef](#)]
18. Sillmann, J.; Kharin, V.V.; Zwiers, F.W.; Zhang, X.; Bronaugh, D. Climate extremes indices in the CMIP5 multimodel ensemble: Part 2. Future climate projections. *J. Geophys. Res.* **2013**, *118*, 2473–2493. [[CrossRef](#)]
19. Donat, M.G.; Alexander, L.V.; Yang, H.; Durre, I.; Vose, R.; Dunn, R.J.H.; Willett, K.M.; Aguilar, E.; Brunet, M.; Caesar, J.; et al. Updated analyses of temperature and precipitation extreme indices since the beginning of the twentieth century: The HadEX2 dataset. *J. Geophys. Res. Atmos.* **2013**, *118*, 2098–2118. [[CrossRef](#)]
20. Nojarov, P. Circulation factors affecting precipitation over Bulgaria. *Theor. Appl. Climatol.* **2017**, *127*, 87–101. [[CrossRef](#)]
21. Casado, M.J.; Pastor, M.A. Circulation types and winter precipitation in Spain. *Int. J. Climatol.* **2016**, *36*, 2727–2742. [[CrossRef](#)]
22. Song, L.; Wang, L.; Chen, W.; Zhang, Y. Intraseasonal variation of the strength of the East Asian Trough and its climatic impacts in Boreal winter. *J. Clim.* **2016**, *29*, 2557–2577. [[CrossRef](#)]
23. Wang, Y.B.; Shi, N. The relationship between the North Atlantic Oscillation anomaly in the recent 45 years and the climate in my country. *Chin. J. Atmos. Sci.* **2001**, *24*, 315–322. (In Chinese) [[CrossRef](#)]
24. Ping, J.H.; Wei, X.H.; Nichol, C. Cumulative Precipitation Departure from Average Characterizing Mountain System Recharge in Semi-arid North Okanagan, South Interior British Columbia, Canada. *J. Appl. Sci.* **2014**, *14*, 2156–2162. [[CrossRef](#)]
25. Deng, H.J.; Chen, Y.N.; Wang, H.J.; Zhang, S.H. Climate change with elevation and its potential impact on water resources in the Tianshan Mountains, Central Asia. *Glob. Planet. Chang.* **2015**, *135*, 28–37. [[CrossRef](#)]
26. Chen, Y.N.; Li, Z.; Fan, Y.T.; Wang, H.J.; Deng, H.J. Progress and prospects of climate change impacts on hydrology in the arid region of northwest China. *Environ. Res.* **2015**, *139*, 11–19. [[CrossRef](#)]
27. Chen, Y.; Li, W.; Deng, H.; Fang, G.; Li, Z. Changes in Central Asia’s Water Tower: Past, Present and Future. *Sci. Rep.* **2016**, *6*, 35458. (In Chinese) [[CrossRef](#)]
28. Wang, S.J.; Yang, Y.D.; Gong, W.Y.; Che, Y.J.; Ma, X.G.; Xie, J. Reason Analysis of the Jiwenco Glacial Lake Outburst Flood (GLOF) and Potential Hazard on the Qinghai-Tibetan Plateau. *Remote Sens.* **2021**, *13*, 3114. [[CrossRef](#)]
29. Zisopoulou, K.; Panagoulia, D. An In-Depth Analysis of Physical Blue and Green Water Scarcity in Agriculture in Terms of Causes and Events and Perceived Amenability to Economic Interpretation. *Water* **2021**, *13*, 1693. [[CrossRef](#)]
30. Xu, J.H.; Chen, Y.N.; Lu, F.; Li, W.H.; Zhang, L.J.; Hong, Y.L. The Nonlinear trend of runoff and its response to climate change in the Aksu River, western China. *Int. J. Climatol.* **2011**, *31*, 687–695. [[CrossRef](#)]

31. Xu, J.H.; Chen, Y.N.; Bai, L.; Xu, Y.W. A hybrid model to simulate the annual runoff of the Kaidu River in northwest China. *Hydrol. Earth Syst. Sci.* **2016**, *20*, 1447–1457. [[CrossRef](#)]
32. Wang, S.J.; Che, Y.J.; Wei, Y.Q. Spatiotemporal Dynamic Characteristics of Typical Temperate Glaciers in China. *Sci. Rep.* **2021**, *11*, 657. [[CrossRef](#)]
33. Rienecker, M.M.; Suarez, M.J.; Todling, R.; Bacmeister, J.; Takacs, L.; Liu, H.-C.; Gu, M.; Sienkiewicz, M.; Koster, R.D.; Gelaro, R.; et al. The GEOS-5 Data Assimilation System—Documentation of versions 5.0.1, 5.1.0, and 5.2.0. In *Technical Report Series on Global Modeling and Data Assimilation*; NASA: Washington, DC, USA, 2008; Volume 27.
34. Dee, D.P.; Uppala, S.M.; Simmons, A.J.; Berrisford, P.; Poli, P.; Kobayashi, S.; Andrae, U.; Balmaseda, M.A.; Balsamo, G.; Bauer, P.; et al. The ERA-Interim reanalysis: Configuration and performance of the data assimilation system. *Q. J. Roy. Meteor. Soc.* **2011**, *137*, 553–597. [[CrossRef](#)]
35. Hersbach, H.; Dee, D. ERA5 Reanalysis Is in Production, ECMWF Newsletter 147-Spring 2016. Available online: <https://www.ecmwf.int/en/newsletter/147/news/era5-reanalysis-production> (accessed on 20 December 2021).
36. Huffman, G.J.; Bolvin, D.T.; Nelkin, E.J.; Wolff, D.B.; Adler, R.F.; Gu, G.; Hong, Y.; Bowman, K.P.; Stocker, E.F. The TRMM Multisatellite Precipitation Analysis (TMPA): Quasi-global, multi-year, combined-sensor precipitation estimates at fine scales. *J. Hydrometeor.* **2007**, *8*, 38–55. [[CrossRef](#)]
37. Huffman, G.J.; Adler, R.F.; Arkin, P.; Chang, A.; Ferraro, R.; Gruber, A.; Janowiak, J.; McNab, A.; Rudolf, B.; Schneider, U. The Global Precipitation Climatology Project (GPCP) Combined Precipitation Dataset. *Bull. Am. Meteorol. Soc.* **1997**, *78*, 5–20. [[CrossRef](#)]
38. Adler, R.F.; Huffman, G.J.; Chang, A.; Farraro, R.; Xie, P.-P.; Janowiak, J.; Rudolf, B.; Schneider, U.; Curtis, S.; Bolvin, D.; et al. The version-2 Global Precipitation Climatology Project (GPCP) monthly precipitation analysis (1979–present). *J. Hydrometeor.* **2003**, *4*, 1147–1167. [[CrossRef](#)]
39. Jiao, D.L.; Xu, N.N.; Yang, F.; Xu, K. Evaluation of spatial-temporal variation performance of ERA5 precipitation data in China. *Sci. Rep.* **2021**, *11*, 17956. [[CrossRef](#)]
40. Zhang, Y.Q.; Mao, G.X.; Chen, C.C.; Shen, L.C.; Xiao, B.Y. Population Exposure to Compound Droughts and Heatwaves in the Observations and ERA5 Reanalysis Data in the Gan River Basin, China. *Land* **2021**, *10*, 1021. [[CrossRef](#)]
41. Song, Y.Y.; Wei, J.F. Diurnal cycle of summer precipitation over the North China Plain and associated land–atmosphere interactions: Evaluation of ERA5 and MERRA-2. *Int. J. Climatol.* **2021**, *41*, 6031–6046. [[CrossRef](#)]
42. Albergel, C.; Dutra, E.; Munier, S.; Calvet, J.C.; Munoz-Sabater, J.; Rosnay, P.d.; Balsamo, G. ERA-5 and ERA-Interim driven ISBA land surface model simulations: Which one performs better? *Hydrol. Earth Syst. Sci.* **2018**, *22*, 3515–3532. [[CrossRef](#)]
43. Crossett, C.C.; Betts, A.K.; Dupigny-Giroux, L.L.; Bombles, A. Evaluation of Daily Precipitation from the ERA5 Global Reanalysis against GHCN Observations in the Northeastern United States. *Climate* **2020**, *8*, 148. [[CrossRef](#)]
44. Zhang, Q.; Shen, Z.X.; Xu, C.Y.; Sun, P.; Hu, P.; He, C.Y. A new statistical downscaling approach for global evaluation of the CMIP5 precipitation outputs: Model development and application. *Sci. Total Environ.* **2019**, *690*, 1048–1067. [[CrossRef](#)]
45. Chen, J.; Brissette, F.P.; Leconte, R. Assessing regression-based statistical approaches for downscaling precipitation over North America. *Hydrol. Process.* **2014**, *28*, 3482–3504. [[CrossRef](#)]
46. Sachindra, D.A.; Ahmed, K.; Rashid, M.M.; Shahid, S.; Perera, B.J.C. Statistical downscaling of precipitation using machine learning techniques. *Atmos. Res.* **2018**, *212*, 240–258. [[CrossRef](#)]
47. Sharifi, E.; Saghafian, B.; Steinacker, R. Downscaling Satellite Precipitation Estimates With Multiple Linear Regression, Artificial Neural Networks, and Spline Interpolation Techniques. *J. Geophys. Res. Atmos.* **2019**, *124*, 789–805. [[CrossRef](#)]
48. Beecham, S.; Rashid, M.; Chowdhury, R.K. Statistical downscaling of multi-site daily rainfall in a south Australian catchment using a generalized linear model. *Int. J. Climatol.* **2014**, *34*, 3654–3670. [[CrossRef](#)]
49. Kueh, S.M.; Kuok, K.K. Precipitation downscaling using the artificial neural network BatNN and development of future rainfall intensity-duration-frequency curves. *Clim. Res.* **2016**, *68*, 73–89. [[CrossRef](#)]
50. Pour, S.H.; Shahid, S.; Chung, E.S.; Wang, X.J. Model output statistics downscaling using support vector machine for the projection of spatial and temporal changes in rainfall of Bangladesh. *Atmos. Res.* **2018**, *213*, 149–162. [[CrossRef](#)]
51. Okkan, U.; Inan, G. Bayesian learning and relevance vector machines approach for downscaling of monthly precipitation. *J. Hydrol. Eng.* **2014**, *20*, 04014051. [[CrossRef](#)]
52. Vandal, T.; Kodra, E.; Ganguly, A.R. Intercomparison of machine learning methods for statistical downscaling: The case of daily and extreme precipitation. *Theor. Appl. Climatol.* **2019**, *137*, 557–570. [[CrossRef](#)]
53. Knopov, P.S.; Kasitskaya, E.I. Consistency of least-square estimates for parameters of the Gaussian regression model. *Cybern. Syst. Anal.* **1999**, *35*, 19–25. [[CrossRef](#)]
54. Xu, W.; Chen, W.; Liang, Y.J. Feasibility study on the least square method for fitting non-Gaussian noise data. *Phys. A Stat. Mech. Appl.* **2018**, *492*, 1917–1930. [[CrossRef](#)]
55. Liu, Y.; Yang, D.K. Convergence analysis of the batch gradient-based neuro-fuzzy learning algorithm with smoothing L1/2 regularization for the first-order Takagi–Sugeno system. *Fuzzy Sets Syst.* **2017**, *319*, 28–49. [[CrossRef](#)]
56. Nakama, T. Theoretical analysis of batch and on-line training for gradient descent learning in neural networks. *Neurocomputing* **2009**, *73*, 151–159. [[CrossRef](#)]
57. Wang, C.; Xu, J.H.; Chen, Y.N.; Bai, L.; Chen, Z.S. A hybrid model to assess the impact of climate variability on streamflow for an ungauged mountainous basin. *Clim. Dyn.* **2017**, *50*, 2829–2844. [[CrossRef](#)]

58. Zuo, J.P.; Xu, J.H.; Chen, Y.N.; Wang, C. Downscaling Precipitation in the DataScarce Inland River Basin of Northwest China based on Earth System Data Products. *Atmosphere* **2019**, *10*, 613. [CrossRef]
59. Aizen, V.B.; Aizen, E.M.; Melack, J.M.; Dozier, J. Climatic and Hydrologic Changes in the Tien Shan, Central Asia. *J. Clim.* **1997**, *10*, 1393–1404. [CrossRef]
60. Wang, S.; Zhang, M.; Hughes, C.; Zhu, X.; Dong, L.; Ren, Z.; Chen, F. Factors controlling stable isotope composition of precipitation in arid conditions: An observation network in the Tianshan Mountains, Central Asia. *Tellus B Chem. Phys. Meteorol.* **2016**, *68*, 26206. [CrossRef]
61. Xu, M.; Kang, S.C.; Wu, H.; Yuan, X. Detection of spatio-temporal variability of air temperature and precipitation based on long term meteorological station observations over Tianshan Mountains, Central Asia. *Atmos. Res.* **2018**, *203*, 141–163. [CrossRef]
62. Tang, Z.G.; Wang, X.R.; Wang, J.; Wang, X.; Li, H.Y.; Jiang, Z.L. Spatiotemporal variation of snow cover in Tianshan mountains, central Asia, based on cloud-free Modis fractional snow cover product, 2001–2015. *Remote Sens.* **2017**, *9*, 1045. [CrossRef]
63. Cai, P.; Hamdi, R.; Luo, G.P.; He, H.L.; Zhang, M.; Termonia, P.; Maeyer, P.D. Agriculture intensification increases summer precipitation in Tianshan Mountains, China. *Atmos. Res.* **2019**, *227*, 140–146. [CrossRef]
64. Fan, M.T.; Xu, J.H.; Chen, Y.N.; Li, W.H. Modeling streamflow driven by climate change in data-scarce mountainous basins. *Sci. Total Environ.* **2021**, *790*, 148256. [CrossRef] [PubMed]
65. Zhang, X. Study on the Downscaling Algorithm of Remote Sensing Precipitation and Analysis of Temporal-Spatial Characteristic in the Middle Section of Mount Tianshan. Master's Thesis, Northwest Normal University, Lanzhou, China, 2013. Available online: <http://cdmd.cnki.com.cn/Article/CDMD-10736-1014019311.htm> (accessed on 20 December 2021). (In Chinese)
66. Rohde, R.A.; Hausfather, Z. The Berkeley Earth Land/Ocean Temperature Record. *Earth Syst. Sci. Data* **2020**, *12*, 3469–3479. [CrossRef]
67. Hou, A.Y. Hadley circulation as a modulator of the extratropical climate. *J. Atmos. Sci.* **1998**, *55*, 2437–2457. [CrossRef]
68. Chen, F.; Chen, J.; Huang, W.; Chen, S.; Huang, X.; Jin, L.; Jia, J.; Zhang, X.; An, C.; Zhang, J.; et al. Westerlies Asia and monsoonal Asia: Spatiotemporal differences in climate change and possible mechanisms on decadal to sub-orbital timescales. *Earth Sci. Rev.* **2019**, *192*, 337–354. [CrossRef]
69. Feng, F.; Li, Z.Q.; Zhang, M.J.; Jin, S.; Dong, Z.W. Deuterium and oxygen 18 in precipitation and atmospheric moisture in the upper Urumqi River Basin, eastern Tianshan Mountains. *Environ. Earth Sci.* **2013**, *68*, 1199–1209. [CrossRef]
70. Kreutz, K.J.; Wake, C.P.; Aizen, V.B.; Cecil, L.D.; Synal, H.A. Seasonal deuterium excess in a Tien Shan ice core: Influence of moisture transport and recycling in Central Asia. *Geophys. Res. Lett.* **2003**, *30*. [CrossRef]
71. Li, B.F.; Li, Y.P.; Chen, Y.N.; Zhang, B.H.; Shi, X. Recent fall Eurasian cooling linked to North Pacific sea surface temperatures and a strengthening Siberian high. *Nat Commun.* **2020**, *11*, 5202. [CrossRef]
72. Mann, H.B. Nonparametric tests against trend. *Econometrica* **1945**, *13*, 245–259. [CrossRef]
73. Kendall, M.G. *Rank Correlation Methods*; Griffin: London, UK, 1975.
74. Thiel, H. A rank-invariant method of linear and polynomial regression analysis. I, II, III. *Nederl. Akad. Wetensch. Proc.* **1950**, *53*, 386–392, 521–525, 1397–1412. [CrossRef]
75. Sen, P.K. Estimates of the regression coefficient based on Kendall's Tau. *J. Am. Stat. Assoc.* **1968**, *63*, 1379–1389. [CrossRef]
76. Pearson, K. VII. Mathematical contributions to the theory of evolution.—III. Regression, heredity, and panmixia. *Philos. Trans. R. Soc. London. Ser. A Contain. Pap. Math. Phys. Character* **1896**, *187*, 253–318. [CrossRef]
77. Wang, J.; Zhang, C.; Chang, M.Z.; He, W.; Lu, X.H.; Fei, S.M.; Lu, G.D. Optimization of Electronic Nose Sensor Array for Tea Aroma Detecting Based on Correlation Coefficient and Cluster Analysis. *Chemosensors* **2021**, *9*, 266. [CrossRef]
78. Wacker, S.; Gröbner, J.; Vuilleumier, L. A method to calculate cloud-free long-wave irradiance at the surface based on radiative transfer modeling and temperature lapse rate estimates. *Theor. Appl. Climatol.* **2014**, *115*, 551–561. [CrossRef]
79. Revadekar, J.; Hameed, S.; Collins, D.F.; Manton, M.J.; Sheikh, M.M.; Borgaonkar, H.P.; Kothawale, D.R.; Adnan, M.M.; Ahmed, A.U.; Ashraf, J.; et al. Impact of altitude and latitude on changes in temperature extremes over South Asia during 1971–2000. *Int. J. Climatol.* **2012**, *33*, 199–209. [CrossRef]
80. Li, Q.X.; Sun, W.B.; Huang, B.Y.; Dong, W.J.; Wang, X.L.; Zhai, P.M.; Jones, P. Consistency of global warming trends strengthened since 1880s. *Sci. Bull.* **2020**, *65*, 1709–1712. [CrossRef]
81. Lindzen, R.S. The Climate Science Isn't Settled. *Wall Str. J.* **2009**. Available online: <https://www.wsj.com/articles/SB10001424052748703939404574567423917025400> (accessed on 20 December 2021).
82. Wigley, T.M.L.; Schlesinger, M.E. Analytical solution for the effect of increasing CO₂ on global mean temperature. *Nature* **1985**, *315*, 649–652. [CrossRef]
83. Lenton, T.M.; Huntingford, C. Global terrestrial carbon storage and uncertainties in its temperature sensitivity examined with a simple model. *Glob. Chang. Biol.* **2003**, *9*, 1333–1352. [CrossRef]
84. Romps, D.M. Response of Tropical Precipitation to Global Warming. *J. Atmos. Sci.* **2011**, *68*, 123–138. [CrossRef]
85. Liu, X.K.; Rao, Z.G.; Zhang, X.J.; Huang, W.; Chen, J.H.; Chen, F.H. Variations in the oxygen isotopic composition of precipitation in the Tianshan Mountains region and their significance for the Westerly circulation. *J. Geogr. Sci.* **2015**, *25*, 801–816. [CrossRef]
86. Cui, A.N.; Lu, H.Y.; Liu, X.Q.; Shen, C.M.; Xu, D.K.; Xu, B.Q.; Wu, N.Q. Tibetan plateau precipitation modulated by the periodically coupled westerlies and Asian monsoon. *Geophys. Res. Lett.* **2021**, *48*, e2020GL091543. [CrossRef]
87. Hurrell, J.W. Decadal trends in the North Atlantic Oscillation: Regional temperatures and precipitation. *Science* **1995**, *269*, 676–679. [CrossRef] [PubMed]

88. Chen, W.; Song, Y.; Huang, H.R. Relationship between stationary planetary wave activity and the East Asian winter monsoon. *J. Geophys. Res. Atmos.* **2005**, *110*, D14110. [[CrossRef](#)]
89. Huang, R.H.; Chen, J.L.; Wang, L.; Lin, Z.D. Characteristics, processes, and causes of the spatio-temporal variabilities of the East Asian monsoon system. *Adv. Atmos. Sci.* **2012**, *29*, 910–942. [[CrossRef](#)]
90. Lu, R.; Dong, B.; Ding, H. Impact of the Atlantic Multidecadal Oscillation on the Asian summer monsoon. *Geophys. Res. Lett.* **2006**, *33*, 194–199. [[CrossRef](#)]
91. Li, S.L.; Bates, G.T. Influence of the Atlantic Multidecadal Oscillation on the winter climate of East China. *Adv. Atmos. Sci.* **2007**, *24*, 126–135. [[CrossRef](#)]
92. He, S.P.; Gao, Y.Q.; Li, F.; Wang, H.J.; He, Y.C. Impact of Arctic Oscillation on the East Asian climate: A review. *Earth Sci. Rev.* **2017**, *164*, 48–62. [[CrossRef](#)]
93. Park, H.J.; Ahn, J.B. Combined effect of the Arctic Oscillation and the Western Pacific pattern on East Asia winter temperature. *Clim. Dyn.* **2016**, *46*, 3205–3221. [[CrossRef](#)]
94. Rigor, I.G.; Colony, R.L.; Martin, S. Variations in surface air temperature observations in the Arctic, 1979–97. *J. Clim.* **2000**, *13*, 896–914. [[CrossRef](#)]
95. Gong, D.Y.; Wang, S.W.; Zhu, J.H. East Asian Winter Monsoon and Arctic Oscillation. *Geophys. Res. Lett.* **2001**, *28*, 2073–2076. [[CrossRef](#)]
96. Sun, J.Q.; Wang, H.J.; Yuan, W. Decadal variations of the relationship between the summer North Atlantic Oscillation and middle East Asian air temperature. *J. Geophys. Res.* **2008**, *113*, D15107. [[CrossRef](#)]
97. Zhao, P.; Zhu, Y.N.; Zhang, R.H. An Asian–Pacific teleconnection in summer tropospheric temperature and associated Asian climate variability. *Clim. Dyn.* **2007**, *29*, 293–303. [[CrossRef](#)]
98. Zhou, B.T.; Zhao, P. Modeling variations of summer upper tropospheric temperature and associated climate over the Asian Pacific region during the mid-Holocene. *J. Geophys. Res.* **2010**, *115*, D20109. [[CrossRef](#)]
99. Petoukhov, V.; Rahmstorf, S.; Petri, S.; Schellnhuber, H.J. Quasiresonant amplification of planetary waves and recent Northern Hemisphere weather extremes. *Proc. Natl Acad. Sci. USA* **2013**, *110*, 5336–5341. [[CrossRef](#)] [[PubMed](#)]
100. Wegmann, M.; Orsolini, Y.; Zolina, O. Warm Arctic–cold Siberia: Comparing the recent and the early 20th-century Arctic warmings. *Environ. Res. Lett.* **2018**, *13*, 025009. [[CrossRef](#)]
101. Tokinaga, H.; Xie, S.P.; Mukougawa, H. Early 20th-century Arctic warming intensified by Pacific and Atlantic multidecadal variability. *Proc. Natl Acad. Sci. USA* **2017**, *114*, 6227–6232. [[CrossRef](#)]
102. Liu, Y.C.; Jiao, K.Q.; Zhao, K.; Liu, Y.; Han, T.D.; Zhong, Y.; Shen, Y.P.; Hao, Y.H.; Ye, B.S. The response of precipitation to global climate change in the Tianshan Mountains, China. *J. Glaciol. Geocryol.* **2017**, *39*, 748–759. (In Chinese) [[CrossRef](#)]
103. Leung, M.Y.T.; Zhou, W. Variation of circulation and East Asian climate associated with anomalous strength and displacement of the East Asian trough. *Clim. Dyn.* **2015**, *45*, 2713–2732. [[CrossRef](#)]
104. Timmermann, A.; An, S.-I.; Kug, J.-S.; Jin, F.-F.; Cai, W.; Capotondi, A.; Cobb, K.M.; Lengaigne, M.; McPhaden, M.J.; Stuecker, M.; et al. El Niño–Southern Oscillation complexity. *Nature* **2018**, *559*, 535–545. [[CrossRef](#)]
105. Zhang, Y.; Xie, S.P.; Kosaka, Y.; Yang, J.C. Pacific Decadal Oscillation: Tropical Pacific forcing versus internal variability. *J. Clim.* **2018**, *31*, 8265–8279. [[CrossRef](#)]
106. Yang, S.; Lau, K.M.; Kim, K.M. Variations of the East Asian jet stream and Asian–Pacific–American winter climate anomalies. *J. Clim.* **2002**, *15*, 306–325. [[CrossRef](#)]
107. Zuo, J.Q.; Li, W.J.; Sun, C.H.; Xu, L.; Ren, H.L. Impact of the North Atlantic sea surface temperature tripole on the East Asian Summer Monsoon. *Adv. Atmos. Sci.* **2013**, *30*, 1173–1186. [[CrossRef](#)]
108. Zheng, F.; Li, J.P.; Li, Y.J.; Zhao, S.; Deng, D.F. Influence of the summer NAO on the spring-NAO-based predictability of the East Asian Summer Monsoon. *J. Appl. Meteor. Climatol.* **2016**, *55*, 1459–1476. [[CrossRef](#)]
109. Qiao, S.B.; Gong, Z.Q.; Feng, G.L.; Qian, Z.H. Relationship between cold winters over Northern Asia and the subsequent hot summers over mid-lower reaches of the Yangtze River valley under global warming. *Atmos. Sci. Lett.* **2015**, *16*, 479–484. [[CrossRef](#)]
110. Henderson, G.R.; Peings, Y.; Furtado, J.C.; Kushner, P.J. Snow–atmosphere coupling in the Northern Hemisphere. *Nat. Clim. Chang.* **2018**, *8*, 954–963. [[CrossRef](#)]
111. Tyrlis, E.; Manzini, E.; Bader, J.; Ukita, J.; Nakamura, H.; Matei, D. Ural blocking driving extreme Arctic sea ice loss, cold Eurasia, and stratospheric vortex weakening in autumn and early winter 2016–2017. *J. Geophys. Res.* **2019**, *124*, 11313–11329. [[CrossRef](#)]
112. Wegmann, M.; Rohrer, M.; Santolaria-Otín, M.; Lohmann, G. Eurasian autumn snow link to winter North Atlantic Oscillation is strongest for Arctic warming periods. *Earth Syst. Dynam.* **2020**, *11*, 509–524. [[CrossRef](#)]